

2 | Strong lensing analysis of PLCK G004.5–19.5 at $z = 0.52$

The recent discovery of a large number of galaxy clusters using the Sunyaev-Zel'dovich (SZ) effect has opened a new era on the study of the most massive clusters in the Universe. Multi-wavelength analyses are required to understand the properties of these new sets of clusters, which are a sensitive probe of cosmology. We aim at a multi-wavelength characterization of PLCK G004.5–19.5, one of the most massive X-ray validated SZ effect–selected galaxy clusters discovered by the *Planck* satellite. We have observed PLCK G004.5–19.5 with GMOS on the 8.1m-Gemini South Telescope for optical imaging and spectroscopy, and performed a strong lensing analysis. We also searched for associated radio emission in published catalogs. An analysis of the optical images confirms that this is a massive cluster, with a dominant central galaxy (the BCG) and an accompanying red sequence of galaxies, plus a $14''$ -long strong lensing arc. Longslit spectroscopy of 6 cluster members shows that the cluster is at $z = 0.516 \pm 0.002$. We also targeted the strongly lensed arc, and found $z_{\text{arc}} = 1.601$. We use LensTool to carry out a strong lensing analysis, from which we measure a median Einstein radius $\theta_E(z_s = 1.6) \simeq 30''$ and estimate an enclosed mass $M_E = 2.45^{+0.45}_{-0.47} \times 10^{14} M_\odot$. By extrapolating an NFW profile we find a total mass M_{200} . Including a constraint on the mass from previous X-ray observations yields a slightly higher mass, $M_{500}^{\text{SL+X}} = 6.7^{+2.6}_{-1.3} \times 10^{14} M_\odot$, consistent with the value from strong lensing alone. High-resolution radio images from the TIFR GMRT Sky Survey at 150 MHz reveal that PLCK G004.5–19.5 hosts a powerful radio relic on scales $\lesssim 500$ kpc. Emission at the same location is also detected in low resolution images at 843 MHz and 1.4 GHz. This is one of the higher redshift radio relics known to date.

2.1 Introduction

In the last few years, the Sunyaev-Zel’dovich (SZ) effect has proven to be an effective method to find massive galaxy clusters at all redshifts, with results from the Atacama Cosmology Telescope (ACT, e.g., [Marriage et al. 2011](#); [Hasselfield et al. 2013](#)), the South Pole Telescope (SPT, e.g., [Williamson et al. 2011](#); [Reichardt et al. 2013](#)) and the *Planck* satellite (e.g., [Planck Collaboration 2011a, 2014](#)) already yielding a few hundred newly discovered clusters up to $z \sim 1.4$. The SZ effect is a distortion in the Cosmic Microwave Background (CMB) spectrum in the direction of galaxy clusters caused by inverse Compton scattering of CMB photons by the hot electrons in the intracluster gas ([Sunyaev & Zel’dovich 1972](#)). Multi-wavelength follow-up observations of SZ-selected clusters have confirmed the unique potential of the SZ effect for detecting the most massive clusters in the Universe (e.g., [Benson et al. 2013](#); [Sifón et al. 2013](#)), with the SZ-discovered El Gordo and SPT-CL J2344–4243 being two of the most extreme galaxy clusters ever known ([Menanteau et al. 2012](#); [McDonald et al. 2012](#)). As expected, many of these clusters display strong lensing features ([Menanteau et al. 2010b](#)), a good indication that these are very massive systems.

Observations of these strongly lensed background galaxies offer one of the most robust ways of constraining the mass of a cluster, providing a direct measure of the mass within the Einstein radius (see [Kneib & Natarajan 2011](#), for a recent review). In combination with other probes (such as X-rays and weak lensing), strong lensing analyses have provided some of the most complete mass distribution models for galaxy clusters, even allowing for the determination of the 3-dimensional configuration in some cases (e.g., [Morandi et al. 2010](#); [Limousin et al. 2013](#)).

Here, we present a multi-wavelength analysis of *PLCK G004.5–19.5*, one of the most massive, hot and X-ray luminous galaxy clusters discovered by the *Planck* satellite via the SZ effect and validated with *XMM-Newton* X-ray observations ([Planck Collaboration 2011b](#)). We perform a strong lensing analysis from optical imaging and spectroscopy, and show from archival radio imaging that *PLCK G004.5–19.5* hosts a powerful radio relic.

All uncertainties are quoted at the 68.3% (1σ) confidence level. We assume a flat Λ CDM cosmology with $\Omega_M = 0.3$ and $H_0 = 70 \text{ km s}^{-1} \text{ Mpc}^{-1}$. Total masses, X-ray and SZ measurements are reported within a radius r_{500} , which encloses a mean density 500 times the critical density of the Universe at the corresponding redshift. All quantities reported by [Planck Collaboration \(2011b\)](#) (reproduced in [Sec. 2.2.1](#)) have been corrected to the spectroscopic redshift $z = 0.516$. All magnitudes are in the AB system.

2.2 Observations and data analysis

2.2.1 SZ and X-ray data

PLCK G004.5–19.5 was discovered through its SZ effect by the *Planck* satellite. With a signal-to-noise ratio (S/N) of 5.9 in the Early Science release, it is just below the S/N threshold of 6.0 set for the *Planck* Early SZ sample (Planck Collaboration 2011a)¹. Despite this relatively low S/N, it has a strong integrated SZ signal, $Y_{500} = (1.90 \pm 0.19) \times 10^{-4} \text{ Mpc}^2$, where $Y \equiv \int y d\Omega$. Here, y is the usual Compton parameter and the integral is over the solid angle of the cluster. We use the $Y - M$ scaling relation of Planck Collaboration (2011c) to estimate a mass $M_{500}^{\text{SZ}} = (10.4 \pm 0.7) \times 10^{14} \text{ M}_{\odot}$.

PLCK G004.5–19.5 was subsequently validated using *XMM-Newton* (Planck Collaboration 2011b), which confirmed that it is an extended X-ray source. Moreover, the observed energy of the Fe K emission line allowed a redshift determination $z_{\text{Fe}} = 0.54$, making it the highest-redshift cluster of the initial *Planck*–*XMM-Newton* validation program. The X-ray analysis of Planck Collaboration (2011b) proves that PLCK G004.5–19.5 is a hot, massive cluster, with an X-ray luminosity² (in the [0.1–2.4] keV band) of $L_{\text{X}} = 1.6 \times 10^{45} \text{ erg s}^{-1}$, an integrated temperature $kT_{\text{X}} = 10.2 \pm 0.5 \text{ keV}$ and a gas mass $M_{\text{gas}} = 1.3 \times 10^{14} \text{ M}_{\odot}$. Combined, the latter two give a pseudo-Compton parameter $Y_{\text{X}} \equiv kT_{\text{X}} M_{\text{gas}} = (13.3 \pm 0.9) \times 10^{14} \text{ M}_{\odot} \text{ keV}$. With this latter value, Planck Collaboration (2011b) estimate a total mass $M_{500}^{\text{X}} = (9.6 \pm 0.5) \times 10^{14} \text{ M}_{\odot}$.

2.2.2 Optical imaging

PLCK G004.5–19.5 was observed on UT 2012 July 19 with the *gri* filters with GMOS on the Gemini-South Telescope (ObsID:GS-2012A-C-1, PI:Menanteau), with exposure times of $8 \times 60 \text{ s}$, $8 \times 90 \text{ s}$ and $8 \times 150 \text{ s}$ respectively. Observations were performed with photometric conditions and seeing $\sim 0.''6$. Images were coadded using SWarp (Bertin et al. 2002) and photometry was performed using SExtractor (Bertin & Arnouts 1996) in dual mode, using the *i*-band for detection. Figure 2.1 shows the combined *gri* image³ of PLCK G004.5–19.5, which shows clearly that there is an overdensity of red elliptical galaxies with a central dominant Brightest Cluster Galaxy (BCG) close to the X-ray peak. Figure 2.1 also reveals the

¹PLCK G004.5–19.5 has been included in the new *Planck* SZ catalog (Planck Collaboration 2014) with a S/N of 6.15.

²The uncertainties in the X-ray values from Planck Collaboration (2011b) do not include systematic errors and have been dropped when negligible.

³Created with stiff (Bertin 2012).

presence of several strong lensing features, most notably a giant arc to the West of the BCG, roughly $14''$ long.

Each galaxy is assigned a photometric redshift by fitting Spectral Energy Distributions (SEDs) to the *gri* photometry using the BPZ code (Benítez 2000) including correction for galactic extinction as described in Menanteau et al. (2010b,a). Typical uncertainties are $\delta z / (1 + z) \simeq 0.09$. The photometric redshift of the cluster, $z_{\text{phot}} = 0.51 \pm 0.02$, was estimated as in Menanteau et al. (2010b,a) and is consistent with the spectroscopic redshift (Sec. 2.2.3). We consider as cluster members all galaxies within $\Delta z = 0.03(1 + z_0) = 0.045$ of $z_0 = 0.51$ and brighter than $m^* + 2 \simeq 22.9$ in the *i*-band, for a total 222 photometrically-selected members. (Here m^* is the characteristic luminosity of the Schechter (1976) function as found by Blanton et al. (2003), passively evolved to z_0 .⁴) Selecting galaxies from a color-magnitude diagram instead or imposing a brighter membership cut have no influence on the results.

2.2.3 Optical spectroscopy

We performed longslit spectroscopy of PLCK G004.5–19.5 on UT 2012 July 20 with GMOS, with $0''.75$ -wide slits with three pointings, two aimed at confirming cluster members and one targeting the most prominent strongly lensed background galaxy. The data were reduced using PyGMOS⁵ (Sifón et al. 2013), with an average wavelength calibration root-mean-square (rms) uncertainty of 0.4\AA . Redshifts were measured by cross-correlating the spectra with Sloan Digital Sky Survey (Abazajian et al. 2009) template spectra using the IRAF package RVSAO (?). The six confirmed cluster members are listed in Table 2.1 and are shown in Figure 2.1 by green circles. They are all red, passive elliptical galaxies and have a rest-frame velocity dispersion $\sigma \sim 860 \text{ km s}^{-1}$ (which is likely not representative of the cluster velocity dispersion). The median redshift of these 6 members, $z = 0.516 \pm 0.002$, is adopted as the cluster redshift (with uncertainties given by $\sigma \sqrt{\pi/2N}$).

The left panel of Figure 2.2 shows a zoomed-in view of the brightest lensed galaxy. Two brightness peaks can be identified, which we interpret as two blended strong lensing images of a single source (see Sec. 2.3). The top-right panel shows the 2d spectrum along the arc, where a faint continuum can be distinguished between the north and south images. The red inset histogram shows the normalized counts for each row over the spectral range shown, after an iterative 3σ -clipping rejection so that bad pixels and emission lines are not included in the counts. This histogram shows that the decrease in brightness is significant between the two peaks but that this region is, in turn, still detected at high significance.

⁴For reference, the BCG has a luminosity $L = 9.5L^*$.

⁵<http://www.strw.leidenuniv.nl/~sifon/pygmoss/>

Table 2.1: Spectroscopically confirmed cluster members.

ID	RA (hh:mm:ss)	Dec (dd:mm:ss)	i mag ^a (AB mag)	Redshift ^b
1 ^c	19:17:05.08	−33:31:20.6	18.47	0.5199 ± 0.0005
2	19:17:07.80	−33:31:31.2	19.74	0.5126 ± 0.0005
3	19:17:08.98	−33:31:48.4	19.16	0.5074 ± 0.0004
4	19:17:09.49	−33:31:43.5	19.70	0.5150 ± 0.0003
5	19:17:10.20	−33:31:38.5	19.83	0.5176 ± 0.0003
6	19:17:14.40	−33:31:57.5	20.48	0.5187 ± 0.0002

^aMAG_AUTO from SExtractor. ^bErrors as given by RVSAO. ^cBrightest Cluster Galaxy.

The middle- and bottom-right panels show the 1d spectra of the two brightness peaks. Both spectra clearly show 5 redshifted FeII absorption lines with rest-frame wavelengths 2344.2, 2374.5, 2382.8, 2586.6 and 2600.2 Å. The median redshift of these 5 pairs of lines is $z_{\text{arc}} = 1.6008 \pm 0.0002$. The bottom spectrum also shows three emission lines (seen in the 2d spectrum as well), which correspond to H β and [OIII] $\lambda\lambda$ 4958,5007Å from a foreground compact star-forming galaxy at $z = 0.203$, for which H α emission is also observed but not shown in Figure 2.2. A small, bright, blue blob is indeed seen overlapping with the south knot (just West of the latter), which we interpret as this foreground galaxy.

2.3 Strong lensing analysis

2.3.1 Strong lensing model

The strong lensing analysis was performed using the Markov Chain Monte Carlo (MCMC) code LensTool (Kneib 1993; Jullo et al. 2007), as follows. The cluster is modelled with an ellipsoidal Navarro-Frenk-White (NFW, Navarro et al. 1995) profile for the main halo, plus a truncated Pseudo-Isothermal Elliptical Mass Distribution (PIEMD, Kassiola & Kovner 1993; Kneib et al. 1996) with a constant mass-to-light ratio for the 222 brightest cluster members (see Sec. 2.2.2). A PIEMD halo is modelled by three parameters: the core radius, r_{core} , the size of the halo (the cut-off radius), r_{cut} , and the velocity dispersion, σ_0 , which scale with galaxy luminosity as (Jullo et al. 2007):

$$r_{\text{core}} = r_{\text{core}}^* (L/L^*)^{1/2} \quad (2.1a)$$

$$r_{\text{cut}} = r_{\text{cut}}^* (L/L^*)^{1/2} \quad (2.1b)$$

$$\sigma_0 = \sigma_0^* (L/L^*)^{1/4}, \quad (2.1c)$$

where $L^* = 6.6 \times 10^{10} L_{\odot}$. The total mass of the galaxy is then given by

$$M = (\pi/G) (\sigma_0^*)^2 r_{\text{cut}}^* (L/L^*). \quad (2.2)$$

We fix $r_{\text{core}}^* = 0.3$ kpc, and r_{cut}^* and σ_0^* are free parameters. The centre of the NFW halo is fixed to the peak of the X-ray emission (located at RA=19:17:04.6, Dec=−33:31:21.9; [Planck Collaboration 2011b](#)). Therefore the mass model has six free parameters: four for the main NFW halo and two for the PIEMD haloes.

As can be seen in the red inset histogram of Figure 2.2, there is a decrease in brightness in the middle of the arc in between two prominent brightness peaks. We interpret this as the merging of two images of the background galaxy and use this double-imaged arc with $z_{\text{arc}} = 1.6$ as a constraint for the lens model, and identify a third image of the same source to the North-East of the BCG (labelled 1.3 in Figure 2.1). The positions and photometry of these three images are listed in Table 2.2.

The total mass model is therefore optimized using the 222 brightest members (including the six spectroscopic members) and the three images for the background galaxy at $z = 1.601$. We adopt a positional uncertainty $\Delta \mathbf{x} = 1.''4$ for the multiple images. The goodness-of-fit for the best model is $\chi_{\text{red}}^2/\text{d.o.f.} = 0.15$, with a rms error on the image positions of $0.''22$. The total mass distribution is moderately elongated along the plane of the sky, approximately aligned with the light distribution. The best-fit values for the six free parameters plus the posterior masses and radii are listed in Table 2.3 (see also Sec. 2.3.2).

Following [Meneghetti et al. \(2011\)](#), the Einstein radius is estimated as the median distance of the tangential critical curves to the cluster centre. We find $\theta_E(z_s = 1.6) = 30.''3_{-3.9}^{+1.4}$, corresponding to a physical distance $r_E \simeq 190$ kpc. Assuming a symmetric lens, the mass inside this region is $M_E = 2.45_{-0.47}^{+0.45} \times 10^{14} M_{\odot}$. Integrating the 3-dimensional NFW profile for the main halo, we obtain M_{200} . The corresponding radius, $r_{500}^{\text{SL}} = 0.93_{-0.08}^{+0.16}$ Mpc, is estimated from M_{500} assuming a spherical cluster. We note that the values at r_{500} are an extrapolation of the strong lensing information.

Recently, [Zitrin et al. \(2012\)](#) derived a representative distribution of Einstein radii from a sample of $\sim 10,000$ clusters from the SDSS optically-selected sample of [Hao et al. \(2010\)](#). They found a log-normal Einstein radius distribution with mean and standard deviation $\langle \log(\theta_E^{\text{eq}}/\text{arcsec}) \rangle = 0.73 \pm 0.32$ for background

Table 2.2: Images of the strongly lensed galaxy.

Source	RA	Dec	r mag ^a	$g - r$ ^b
	(hh:mm:ss)	(dd:mm:ss)	(AB mag)	(AB mag)
1.1	19:17:03.14	−33:31:12.5	21.42 ± 0.01	0.40 ± 0.03
1.2	19:17:02.97	−33:31:19.0	21.42 ± 0.01	0.39 ± 0.02
1.3	19:17:06.45	−33:30:50.8	23.75 ± 0.03	0.35 ± 0.05

^aMAG_ISO from SExtractor. ^bDifference of MAG_APER's from SExtractor.

sources at $z_s \sim 2$. For comparison to Zitrin et al. (2012) and others, we estimate the equivalent Einstein radius to be $\theta_E^{\text{eq}}(z_s = 1.6) \simeq 25''$. PLCK G004.5−19.5 is a 2σ outlier from this mean relation; therefore it can be said to be within the 5% strongest lensing clusters in the Universe.

2.3.2 External constraints

We run LensTool again including a prior in the mass, from the X-ray mass estimated by Planck Collaboration (2011b) as implemented by Verdugo et al. (2011). As mentioned in Sec. 2.2.1, however, the reported uncertainties are unrealistically small. As a more realistic estimate, we take the intrinsic scatter in the latest $Y_X - M$ relation by Mahdavi et al. (2013) of 22%, measured by combining weak lensing and X-ray observations. Thus the additional constraint in the total mass is the following Gaussian prior:

$$M_{500}^X = (9.6 \pm 2.1) \times 10^{14} M_\odot \quad (2.3)$$

measured at $r_{500}^X = 1245$ kpc.⁶ The same exercise for the SZ mass, assuming an uncertainty of 18% corresponding to the central value of the intrinsic scatter in the $Y_{\text{SZ}} - M$ measured by Sifón et al. (2013) using dynamical masses and SZ measurements from ACT, gives

$$M_{500}^{\text{SZ}} = (10.4 \pm 1.9) \times 10^{14} M_\odot \quad (2.4)$$

We only use Equation 2.3 because both measurements are very similar and because they are both measured at the same radius, determined from the X-ray scaling relation (Planck Collaboration 2011b) and are therefore not independent. The posterior distributions are shown for various combinations of parameters for the two different models in Figure 2.3, highlighting degeneracies in the strong lensing model.

⁶Note that in LensTool the X-ray constraint to the strong lensing model is given as a fixed mass M at a fixed radius r (with a mass uncertainty), not explicitly as the mass at a given overdensity.

Table 2.3: Marginalized posterior estimates of the strong lensing model with and without the X-ray mass constraint.

Parameter ^a	Symbol	SL	SL+X	units
Main NFW Halo				
Ellipticity	e	$0.40^{+0.07}_{-0.09}$	$0.37^{+0.08}_{-0.07}$	
Position Angle ^b	θ	52^{+7}_{-3}	53^{+2}_{-1}	deg
Scale radius	r_s	$0.10^{+0.17}_{-0.04}$	$0.39^{+0.07}_{-0.08}$	Mpc
Concentration ^c	c_{200}	$4.0^{+5.0}_{-0.8}$	$4.1^{+1.8}_{-0.6}$	
PIEMD Halos				
Cut-off radius	r_{cut}^*	47^{+13}_{-20}	25^{+28}_{-14}	kpc
Velocity dispersion	σ_0^*	225^{+42}_{-23}	106^{+37}_{-53}	km s^{-1}
Derived Parameters				
Einstein Mass	M_E	$2.45^{+0.45}_{-0.47}$	$2.46^{+0.31}_{-0.59}$	$10^{14} M_\odot$
Einstein Radius	r_E	$30.3^{+1.4}_{-3.9}$	$30.0^{+0.6}_{-3.5}$	arcsec
Total Mass	M_{500}	$4.0^{+2.1}_{-1.0}$	$6.7^{+2.6}_{-1.3}$	$10^{14} M_\odot$
Radius	r_{500}	$0.93^{+0.16}_{-0.08}$	$1.10^{+0.14}_{-0.07}$	Mpc

^aAll parameters have uniform priors. ^bPosition angle West of North. ^cThe concentration is defined as $c_{200} = r_{200}/r_s$.

The X-ray constraint pushes the mass to a higher value which is marginally consistent with the strong lensing only (SL) model. Notably, the SL model allows for a low- M_{500} , high- M_E (through a high r_E), high-concentration and low-ellipticity solution which is marginally excluded by the model including the X-ray constraint (SL+X). The marginalized posterior mass is $M_{500}^{\text{SL+X}} = 6.7^{+2.6}_{-1.3} \times 10^{14} M_\odot$. Although the contours are broader in the SL model, the maximum likelihood estimate (MLE) and marginalized 68% range of M_E (and r_E) are mostly unaffected by the inclusion of the X-ray constraint, with a posterior estimate $M_E^{\text{SL+X}} = 2.46^{+0.31}_{-0.59} \times 10^{14} M_\odot$. This is expected, since r_E is directly constrained by the strongly lensed images, independently of the mass profile of the cluster.

2.4 Radio emission

Radio relics and radio haloes are diffuse, non-thermal emission features that have no obvious connection with individual cluster galaxies and are often associated with merging activity in massive clusters of galaxies (see [Feretti et al. 2012](#), for a recent review). We searched for such features around *PLCK G004.5–19.5* in the

high-resolution 150 MHz images of the TIFR GMRT Sky Survey (TGSS)⁷ Data Release 5 and in VizieR⁸ (Ochsenbein et al. 2000) for additional archival data.

Figure 2.4 shows the intensity map at 150 MHz from the TGSS with blue contours at $(3, 5, 7, 15)\sigma$, where $\sigma = 11.9 \text{ mJy beam}^{-1}$ is the background rms level. Green and red contours show 1.4 GHz and 843 MHz emission from the NRAO VLA Sky Survey (NVSS; Condon et al. 1998) and the Sydney University Molonglo Sky Survey (SUMSS; Mauch et al. 2003), respectively. Both sets of contours are shown at $(3, 5, 10, 20)\sigma$, where $\sigma = 0.51 \text{ mJy beam}^{-1}$ and $2.0 \text{ mJy beam}^{-1}$ in the NVSS and SUMSS images, respectively. There is significant ($> 5\sigma$) emission around PLCK G004.5–19.5 in all three frequencies at coincident locations. Moreover, this emission is extended in the TGSS and NVSS images.

We identify a tangentially extended radio relic in the TGSS image, coincident with emission at the other frequencies, although this emission is barely resolved in SUMSS and NVSS (the extent of the emission is roughly 2 beams in both low-resolution images). The multi-frequency properties of this relic are given in Table 2.4. Radio relics span a wide range of spectral indices, α (where $F_\nu \propto \nu^{-\alpha}$), from $\alpha \sim 1$ up to $\alpha \sim 3$ (Feretti et al. 2012). We give a preliminary estimate of the integrated spectral index of the relic by fitting a power-law to the 150 MHz flux combined with NVSS and SUMSS, one at a time. From both combinations we measure $0.9 \lesssim \alpha \lesssim 1.4$ at the 68% level. Measuring the spectral index from all three frequencies gives a shallower but consistent spectral index $\alpha \sim 0.7 - 1.1$, suggesting that the emission at 843 MHz and/or 1.4 GHz may be contaminated by unresolved point sources, thus boosting the flux and lowering α . A spectral index measured using both 843 MHz and 1.4 GHz would be more affected by this contamination since these two frequencies are closer together (in log-space) than any of them is to the TGSS frequency.

We confirm that there are no X-ray point sources associated with any of the radio emission from the *XMM-Newton* image. As with the relic, sources A, B, C and E have no counterparts in the optical images, nor in the Near Infrared (NIR) from the 2 Micron All Sky Survey (2MASS, Skrutskie et al. 2006) or the Mid Infrared (MIR) from the Wide-field Infrared Survey Explorer All Sky Survey (WISE, Wright et al. 2010), within their nominal position uncertainties. Source D has two plausible counterparts from the 2MASS and WISE (merged into one source) catalogs. Both are stars, and are also seen in our optical images. It is therefore likely that source D is a radio point source. Given its high flux and shape in the TGSS image, source A is also likely a point source, or two blended point sources.

Because the relic elongation is approximately in the same direction as the TGSS

⁷<http://tgss.ncra.tifr.res.in/>

⁸<http://vizier.u-strasbg.fr/viz-bin/VizieR>

beam and source E, we use source E (which can be regarded as noise-dominated, being much less significant and not detected at any other frequency) as a control for the significance of the relic accounting for the TGSS beam. As seen from Tables 2.4 and 2.5, both the relic and source E have similar sizes and position angles. Figure 2.4 shows however that the relic is much more significant than source E. Moreover, the following exercise shows that in the case of source E, the large size is a consequence of the background noise and the beam, whereas the source we associate to the radio relic is significantly extended over the background. We re-measured fluxes for these two sources on images in which we masked all pixels with values below $3\sigma = 35.7 \text{ mJy beam}^{-1}$. More than half the emission associated with source E comes from pixels with $< 3\sigma$ emission, and the major axis is halved in this masked map. From the relic, in contrast, we still measure $\sim 70\%$ of the total flux, and the major axis is 75% of the size measured in the original map.

2.5 Conclusions

We present a multi-wavelength analysis of PLCK G004.5–19.5, one of the massive galaxy clusters recently discovered by the *Planck* satellite using the SZ effect. Optical confirmation from GMOS imaging clearly shows a red sequence of galaxies with a dominant BCG, both undisputable characteristics of galaxy clusters. There is also a strongly lensed giant arc which is composed of two partially merged images of a background galaxy. Spectroscopy of 6 cluster members plus the giant arc show that the cluster is at $z = 0.516 \pm 0.002$ and that the arc is at $z_{\text{arc}} = 1.601$. With these data we have performed a strong lensing analysis, confirming a third image for the source producing the arc. We use LensTool to obtain a mass model for the cluster including the contribution from cluster galaxies, and estimate an Einstein mass $M_E = 2.45^{+0.45}_{-0.47} \times 10^{14} M_\odot$, within a median Einstein ring $r_E \simeq 190 \text{ kpc}$, corresponding to an angular size $\theta_E(z_s = 1.6) \simeq 30''$. Compared to the universal Einstein ring distribution derived by Zitrin et al. (2012), PLCK G004.5–19.5 is among the 5% strongest gravitational lenses in the Universe. By integrating the 3-dimensional NFW profile we estimate M_{200} . We also run LensTool including a Gaussian prior for the X-ray mass estimated by Planck Collaboration (2011b) and find $M_{500}^{\text{SL+X}} = 6.7^{+2.6}_{-1.3} \times 10^{14} M_\odot$, marginally consistent with the mass estimated from strong lensing alone. The Einstein mass does not change significantly when including the X-ray constraint, because the latter is constrained directly by the strongly lensed galaxy. The inclusion of the X-ray mass constraint does help to exclude a high-mass, low-concentration solution which is allowed by the strong lensing-only model.

Examination of archival high-resolution radio data from the TIFR GMRT Sky

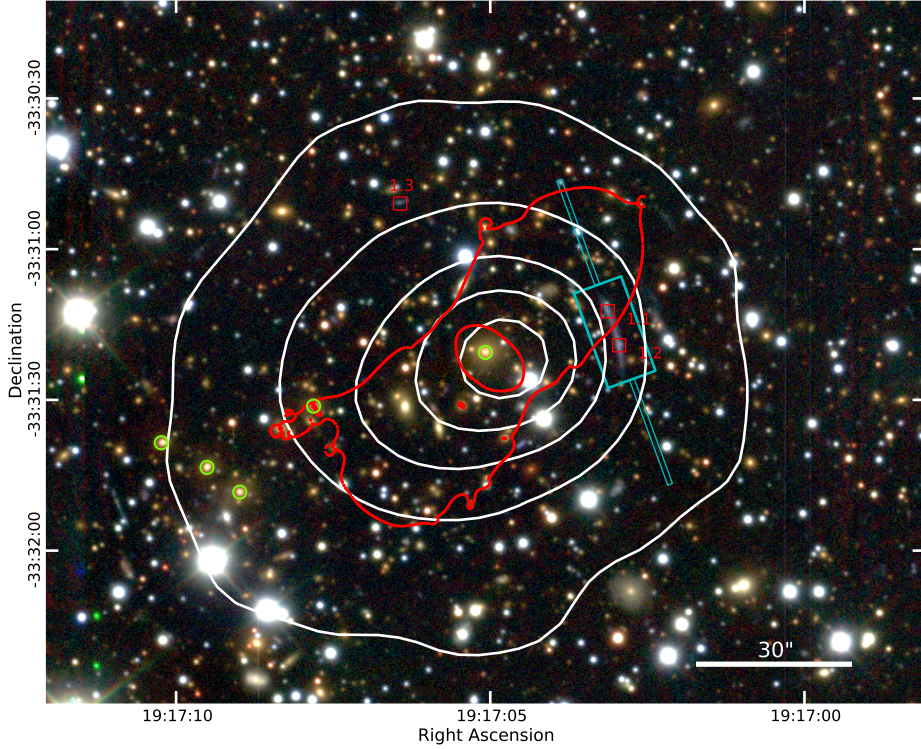


Figure 2.1: GMOS *gri* pseudo-color image of the central region of PLCK G004.5–19.5. North is up, east is left. X-ray surface brightness contours from *XMM-Newton* are overlaid in white. Spectroscopic cluster members are marked by green circles; only 5 out of 6 are visible in the shown region, the sixth member is ~ 760 kpc to the E-SE of the BCG. Red squares mark the position of the 3 confirmed multiple images, while we show in red the critical curve for $z_s = 1.6$. The thin cyan box shows the slit used to get the spectrum of the arc ($1''$ across) ; the wide cyan box shows the region zoomed-in in the left panel of Figure 2.2. The thick white line in the bottom right shows a $30''$ scale, corresponding to 188 kpc at $z = 0.516$.

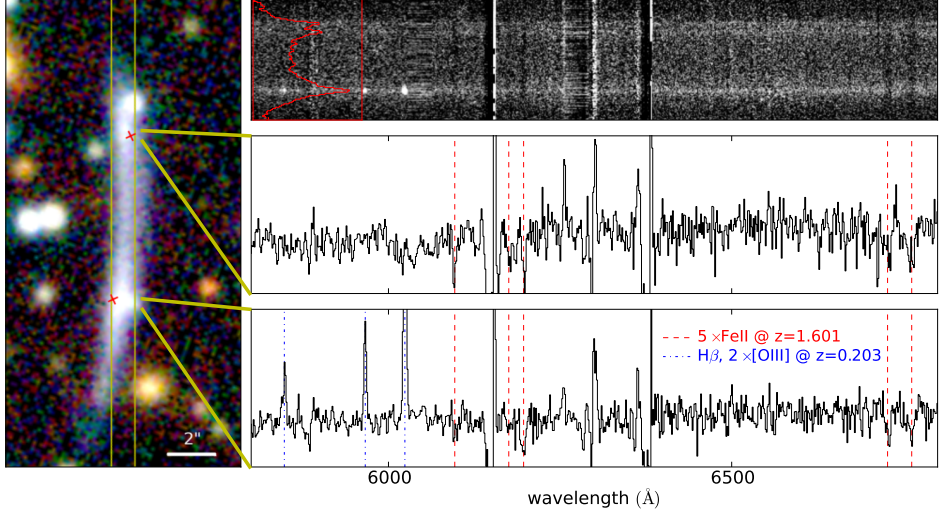


Figure 2.2: Strong lensing giant arc. The left panel shows a $10'' \times 20''$ close-up *gri* image of the arc (cyan box in Figure 2.1), with the red crosses marking the location where *LensTool* predicts the images to be. The thin yellow lines outline the position of the slit and the thick yellow lines mark the approximate locations of the knots from where the 1D spectra are shown. The right panels show the arc spectrum in the wavelength range 5800 – 6800. The top right panel shows the GMOS 2d spectrum. The image is 105 pixels, corresponding to $15''.3$, from top to bottom. The red histogram (inset) shows the total counts in each row over the shown spectral range, after an iterative 3σ -clipping to remove bad pixels and emission lines. This highlights the decrease in brightness (and the significance of the continuum) between the two images. The middle and bottom panels show, respectively, the 1d spectra of the northern (source 1.1) and southern (source 1.2) peaks seen in the lensed arc, each marked by a yellow “wedge” in the left panel. In these, the red dashed lines mark the 5 FeII absorption lines at $z = 1.601$ and the blue dash-dotted lines mark the emission lines from a foreground galaxy at $z = 0.203$, only seen in the south spectrum. The vertical axes in these two panels are in arbitrary units.

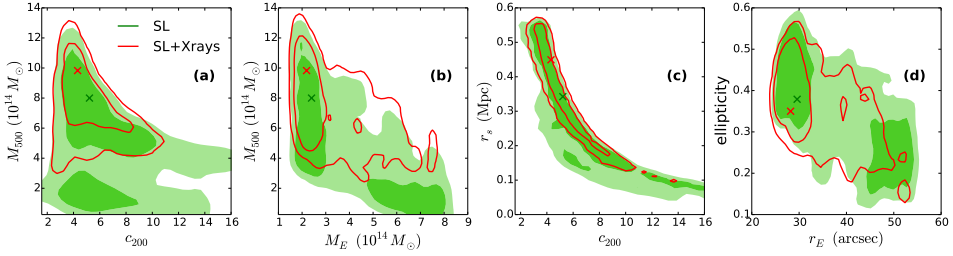


Figure 2.3: Joint 2D posterior distributions of c_{200} and M_{500} (panel a), M_E and M_{500} (panel b), c_{200} and r_s (panel c), and r_E and θ (panel d). Contours are at the 68% and 95% levels. Filled green contours show constraints from strong lensing alone and red contours show the constraints when M_{500}^X is included as an independent constraint. Crosses show the corresponding maximum likelihood estimates.

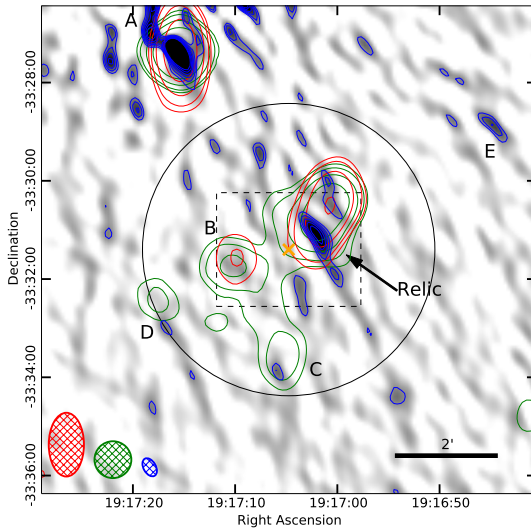


Figure 2.4: $10' \times 10'$ TGSS 150 MHz intensity map around PLCK G004.5–19.5, with contours in blue. Contours are shown at 3, 5, 7 and 15 times σ , where σ is the background rms. NVSS 1.4 GHz and SUMSS 843 MHz contours are shown in green and red, respectively. Both contour sets are in units of 3, 5, 10 and 20 times each σ . The orange cross shows the position of the BCG. The dashed black rectangle is the region shown in Figure 2.1 and the black circle marks $r_{500}^{SL+X} = 1.12$ Mpc. The black bar in the bottom right marks a scale of $2'$. The SUMSS, NVSS and TGSS beams are shown from left to right, respectively, in the bottom left corner (hatched ellipses).

Table 2.4: Radio Relic

Source Name	RA ^a (hh:mm:ss)	Dec ^a (dd:mm:ss)	Freq. (MHz)	Beam ('' \times '')	F_ν ^b (mJy)	Size ^c ('' \times '')	P.A. ^d (deg)
GMRT173_01 ^e	19:17:01.94	−33:31:12.6	150	24 \times 15	382 \pm 80	84 \times 19	28 \pm 5
SUMSS J191701−333033	19:17:01.50(16)	−33:30:33.7(2.5)	843	51 \times 43	51 \pm 4	70 \times 62	136 \pm 3
NVSS 1917101−333035	19:17:01.75(08)	−33:30:35.6(1.3)	1400	45 \times 45	37 \pm 2	74 \times 50	146 \pm 1

^aNominal uncertainties on the last two digits in parentheses. ^bIntegrated Flux. ^cMajor and minor axes. ^dPosition angle West of North. ^ePosition uncertainties from TGSS are $\sim 4''$.

Table 2.5: Other Sources in the Radio Images.

Source	Name	RA (hh:mm:ss)	Dec (dd:mm:ss)	F_ν (mJy)	Size ('' \times '')	P.A. (deg)
A	GMRT243_01 ^{a,b}	19:17:16.71	−33:27:11.8	540 \pm 75	39 \times 19	43
	NVSS J191715−332722	19:17:15.89(05)	−33:27:22.2(0.7)	35.7 \pm 0.5	47 \times 45	176
	SUMSS J191715−332720	19:17:15.75(11)	−33:27:20.6(2.0)	71.5 \pm 2.7	73 \times 49	165
B	NVSS J191710−333144	19:17:10.90(28)	−33:31:44.7(3.3)	11.2 \pm 0.8	74 \times 55	102
	SUMSS J191710−333139 ^c	19:17:10.55(37)	−33:31:39.0(4.6)	8.8 \pm 1.0	57 \times 52	3
C	NVSS J191705−333333	19:17:05.94(32)	−33:33:33.6(8.0)	7.7 \pm 0.5	81 \times 49	173
D	NVSS J191717−333224	19:17:17.84(52)	−33:32:24.4(5.7)	3.7 \pm 0.1	57 \times 42	132
E	GMRT163_01 ^b	19:16:45.13	−33:28:48.9	161 \pm 41	71 \times 14	34

See Notes in Table 2.4. ^aBlended in the TGSS catalog. ^bPosition uncertainties from TGSS are $\sim 4''$. ^cNot in the SUMSS catalog.

Survey at 150 MHz reveals the presence of a radio relic at approximately 250 kpc from the cluster centre. Significant emission is also detected in low-resolution images from NVSS at 1.4 GHz and SUMSS at 843 MHz. A preliminary measurement of the integrated spectral index yields $\alpha \sim 0.9 - 1.4$. We find no detectable point sources contributing significantly to the radio emission in the *XMM-Newton* or Gemini images, nor from archival observations in the NIR or MIR. This radio emission likely originated from recent merging activity, but the available data do not allow for a detailed study of possible merging events. The origin of the radio emission will be addressed with future observations.

Bibliography

- Abazajian K. N., et al., 2009, *ApJS*, **182**, 543
- Benítez N., 2000, *ApJ*, **536**, 571
- Benson B. A., et al., 2013, *ApJ*, **763**, 147
- Bertin E., 2012, in Ballester P., Egret D., Lorente N. P. F., eds, *Astronomical Society of the Pacific Conference Series Vol. 461, Astronomical Data Analysis Software and Systems XXI*. p. 263
- Bertin E., Arnouts S., 1996, *A&AS*, **117**, 393
- Bertin E., Mellier Y., Radovich M., Missonnier G., Didelon P., Morin B., 2002, in Bohlender D. A., Durand D., Handley T. H., eds, *Astronomical Society of the Pacific Conference Series Vol. 281, Astronomical Data Analysis Software and Systems XI*. p. 228
- Blanton M. R., et al., 2003, *ApJ*, **592**, 819
- Condon J. J., Cotton W. D., Greisen E. W., Yin Q. F., Perley R. A., Taylor G. B., Broderick J. J., 1998, *AJ*, **115**, 1693
- Feretti L., Giovannini G., Govoni F., Murgia M., 2012, *A&ARv*, **20**, 54
- Hao J., et al., 2010, *ApJS*, **191**, 254
- Hasselfield M., et al., 2013, *JCAP*, **7**, 008
- Jullo E., Kneib J.-P., Limousin M., Elíasdóttir Á., Marshall P. J., Verdugo T., 2007, *New Journal of Physics*, **9**, 447
- Kassiola A., Kovner I., 1993, *ApJ*, **417**, 450
- Kneib J.-P., 1993, PhD thesis, Ph. D. thesis, Université Paul Sabatier, Toulouse, (1993)
- Kneib J.-P., Natarajan P., 2011, *A&ARv*, **19**, 47
- Kneib J.-P., Ellis R. S., Smail I., Couch W. J., Sharples R. M., 1996, *ApJ*, **471**, 643
- Limousin M., Morandi A., Sereno M., Meneghetti M., Ettori S., Bartelmann M., Verdugo T., 2013, *Space Sci. Rev.*, **177**, 155
- Mahdavi A., Hoekstra H., Babul A., Bildfell C., Jeltema T., Henry J. P., 2013, *ApJ*, **767**, 116
- Marriage T. A., et al., 2011, *ApJ*, **737**, 61
- Mauch T., Murphy T., Buttery H. J., Curran J., Hunstead R. W., Piestrzynski B., Robertson J. G., Sadler E. M., 2003, *MNRAS*, **342**, 1117
- McDonald M., et al., 2012, *Nature*, **488**, 349
- Menanteau F., et al., 2010a, *ApJS*, **191**, 340

- Menanteau F., et al., 2010b, *ApJ*, **723**, 1523
- Menanteau F., et al., 2012, *ApJ*, **748**, 7
- Meneghetti M., Fedeli C., Zitrin A., Bartelmann M., Broadhurst T., Gottlöber S., Moscardini L., Yepes G., 2011, *A&A*, **530**, A17
- Morandi A., Pedersen K., Limousin M., 2010, *ApJ*, **713**, 491
- Navarro J. F., Frenk C. S., White S. D. M., 1995, *MNRAS*, **275**, 720
- Ochsenbein F., Bauer P., Marcout J., 2000, *A&AS*, **143**, 23
- Planck Collaboration 2011a, *A&A*, **536**, A8
- Planck Collaboration 2011b, *A&A*, **536**, A9
- Planck Collaboration 2011c, *A&A*, **536**, A11
- Planck Collaboration 2014, *A&A*, **571**, A29
- Reichardt C. L., et al., 2013, *ApJ*, **763**, 127
- Schechter P., 1976, *ApJ*, **203**, 297
- Sifón C., et al., 2013, *ApJ*, **772**, 25
- Skrutskie M. F., et al., 2006, *AJ*, **131**, 1163
- Sunyaev R. A., Zel'dovich Y. B., 1972, *Comments on Astrophysics and Space Physics*, **4**, 173
- Verdugo T., Motta V., Muñoz R. P., Limousin M., Cabanac R., Richard J., 2011, *A&A*, **527**, A124
- Williamson R., et al., 2011, *ApJ*, **738**, 139
- Wright E. L., et al., 2010, *AJ*, **140**, 1868
- Zitrin A., Broadhurst T., Bartelmann M., Rephaeli Y., Oguri M., Benítez N., Hao J., Umetsu K., 2012, *MNRAS*, **423**, 2308